

Microstructural evolution and mechanical properties of in situ nano Ta₄HfC₅ reinforced SiBCN composite ceramics

Bingzhu Wang

Harbin Institute of Technology

Li Daxin (✉ lidaxin@hit.edu.cn)

Harbin Institute of Technology <https://orcid.org/0000-0003-4930-0031>

Zhihua Yang

Harbin Institute of Technology

Dechang Jia

Harbin Institute of Technology

Jingyi Guan

Harbin Institute of Technology

Hao Peng

Harbin Institute of Technology

Delong Cai

Harbin Institute of Technology

Peigang He

Harbin Institute of Technology

Xiaoming Duan

Harbin Institute of Technology

Yu Zhou

Harbin Institute of Technology

Research Article

Keywords: Ta₄HfC₅; SiBCN; Microstructure evolution; Mechanical properties

Posted Date: March 18th, 2020

DOI: <https://doi.org/10.21203/rs.3.rs-17623/v1>

License:   This work is licensed under a Creative Commons Attribution 4.0 International License.

[Read Full License](#)

Version of Record: A version of this preprint was published at Journal of Advanced Ceramics on November 27th, 2020. See the published version at <https://doi.org/10.1007/s40145-020-0410-9>.

Abstract

In this paper, the in situ nano Ta₄HfC₅ reinforced SiBCN-Ta₄HfC₅ composite ceramics were prepared by a combination of two-step mechanical alloying and reactive hot-pressing sintering. The microstructural evolution and mechanical properties of the SiBCN-Ta₄HfC₅ were studied. After the first-step milling of 30 h, the raw materials of TaC and HfC undergone crushing, cold sintering and short-range interdiffusion to finally obtain the high pure nano Ta₄HfC₅. A hybrid structure of amorphous SiBCN and nano Ta₄HfC₅ was obtained by adopting a second-step ball-milling. After reactive hot-pressing sintering, amorphous SiBCN has crystallized to nano SiC and turbostratic BN(C) phases while Ta₄HfC₅ retained the form of nano structure. With the in situ generation of 2.5 wt% Ta₄HfC₅, Ta₄HfC₅ is preferentially distributed within the turbostratic BN(C); however, as Ta₄HfC₅ content further raised to 10 wt%, it mainly distributed in the grain-boundary of BN(C) and SiC. The introduction of Ta₄HfC₅ nanocrystals can effectively improve the flexural strength and fracture toughness of SiBCN ceramics, reaching to 344.1 MPa and 4.52 MPa·m^{1/2}, respectively.

Introduction

With the development of aerospace technology, more stringent properties requirements are put forward for advanced structural-functional integration ceramic materials^[1]. Among many high-temperature structural materials, SiBCN non-oxide ceramics have attracted considerable attention due to their light-weight, high specific strength, excellent thermal stability and resistance to thermal shock, oxidation and ablation^[2-7].

Polymer/precursor derived ceramics (PDCs) is one of the first routes to prepare SiBCN materials. The SiBCN materials are able to remain amorphous nature at least up to 1400 °C, and do not undergo microstructural changes at this temperature^[4]. The chemistry, microstructure and properties of the PDCs SiBCN can be tailored effectively by controlling the initial reagent structure, chemical reaction and processing parameters^[8]. Unfortunately, this method also has some nonnegligible shortcomings that limit its wide applications. The starting materials are usually expensive and some organic solvents used are harmful to human health and the environment. This processing route is also low-yield and complex. During pyrolysis, the gases release and the mass loss are required to be carefully monitored to avoid porous structure and accurately control shrinkage (even microcracks)^[9-11].

Thus, a more efficient, convenient and environment-friendly method was proposed to obtain dense nano or amorphous SiBCN monoliths and their ceramic composites, using a combination of mechanical alloying and solid-state sintering techniques (also referred as inorganic method)^[10]. One of the significant advantages of this processing route is to provide centimeter-sized samples. The centimeter-sized samples are convenient for evaluating the basic mechanical and thermophysical properties^[11-12]. However, the previous studies showed that the heterogeneous microstructure, which leads to poor

mechanical properties of the SiBCN ceramics, are needed to be further optimized for the real applications at high-temperatures [13–14].

As documented, the introduction of ultra-high temperature ceramics (UHTCs) into SiBCN ceramic matrix, is considered to be an effective strategy to improve the mechanical performance of SiBCN ceramics [15–18]. In previous attempts, the microstructural evolution and thermal stability of the porous PDCs ZrB₂-SiBCN and HfN-SiBCN composite ceramics have been investigated [19–20]. But the mechanical properties of these composite ceramics have not been evaluated because of the limitation of sample size. In another contribution, Liang et al. [21–23] have introduced some LaB₆ into SiBCN matrix by the inorganic method, obtaining desirable mechanical properties compared with pure SiBCN. However, during the sintering process, some LaB₆ has reacted with SiBCN ceramic matrix and generated La₂B₂C₆. Consequently, the strengthening and toughening effects of LaB₆ were significantly reduced. Further, Miao et al. [24–26] have prepared SiBCN-ZrB₂ composite ceramics by mechanical alloying combined with the sol-gel method. The results suggested that the in situ ZrB₂ can improve the mechanical properties of SiBCN ceramic materials to some extent; nevertheless, the particle size of the in-situ ZrB₂ has grown up to a maximum value of ~ 1 μm.

Generally, the following factors should be considered when the external UHTCs are selected as reinforcements in SiBCN ceramics: (i) they should not react with SiBCN matrix to form strong bonding interfacial structure during annealing or sintering; (ii) they could be uniformly dispersed in ceramic matrix in the form of nanocrystals and (iii) are supposed to have good physical-chemical compatibility with SiBCN.

The chemically stable Ta₄HfC₅, the current highest melting point compound, was theoretically forecasted by Agte et al. [27] and experimentally confirmed by Andrievskii et al. [28]. Up to present, various strategies have been used to the synthesis of the high pure Ta₄HfC₅. For example, Simonenko et al. [29] have reported a sol-gel technology for preparing Ta₄HfC₅ by using metal oxide and gel of polymeric carbon source. The polymeric carbon source was preliminarily annealing to provide a uniform dispersion of metal oxide-carbon mixture, and then further heating to 1200 ~ 1500 °C to obtain pure Ta₄HfC₅. Liu et al. [30] used the Hf and Ta containing polyantahafnoxane modified with allyl-functional novolac resin to produce Ta₄HfC₅ polymer (polyantahafnoxanesal). The resulting polyantahafnoxanesal is subsequently solidified and pyrolyzed at 1400 °C to obtain pure Ta₄HfC₅. These methods, of course, are quite effective to prepare pure Ta₄HfC₅ with high thermal stability and chemical stability; however, these processing methods often contain complex synthesis steps, resulting in high-cost products. The raw materials used are also flammable and present waste disposal problems. For this reason, Osama et al. [31] have successfully prepared nano Ta₄HfC₅ by mechanical alloying for the first time. However, the formation mechanisms of the mechanical alloying derived nano Ta₄HfC₅ is still unclear. And the research on Ta₄HfC₅/SiBCN composite ceramics has not been reported yet.

Thus, in this work, initially, the Ta₄HfC₅ nanocrystals were prepared by an improving mechanical alloying method and then, nano Ta₄HfC₅ was introduced to the prefabricated amorphous SiBCN powders by a second stage of mechanical alloying. Afterward, the hot-pressing sintering technology was adopted to consolidate SiBCN-Ta₄HfC₅ composite ceramics. The formation mechanisms of mechanical alloying derived nano Ta₄HfC₅, the correlation of microstructural evolution and mechanical properties of the resulting SiBCN-Ta₄HfC₅ composite ceramics were illustrated. As expected, the homogeneous distribution of nano Ta₄HfC₅ within the SiBCN ceramic matrix strongly improved the mechanical properties of the composite ceramics. This work has solved the problems of uneven distribution of ultra-high temperature phases in the ceramic matrix, which is beneficial to the real applications of SiBCN ceramics.

Materials And Methods

Raw materials

Commercial available hexagonal boron nitride (h-BN, 99.0% purity, 0.6 μm, purchased from Advanced Technology & Materials Co., Ltd), graphite (99.5% purity, 8.7 μm, purchased from Qingdao Huatai Lubricant Sealing S&T Co., Ltd), cubic silicon (c-Si, 99.9% purity, 9.0 μm, purchased from China New Metal Materials Technology Co., Ltd.), hafnium carbide (HfC, 99.0% purity, 1 μm, purchased from Shanghai Puwei Applied Materials Technology Co., Ltd) and tantalum carbide (TaC, 99.0% purity, 1 μm, purchased from Shanghai Puwei Applied Materials Technology Co., Ltd) were used here as received.

Synthesis of Ta₄HfC₅ nanocrystals

Ta₄HfC₅ nanocrystals were prepared by mechanical alloying method via a P4 high-energy ball-miller manufactured by FRITSCH company. Firstly, TaC and HfC mixed powders with a molar ratio of 4: 1 were poured into the ball milling tanks filled with argon, and then subjected to different hours of milling. The ball-to-powder mass ratio was set as 20: 1 and the effective ball-milling time was X h (X = 0.5, 1, 1.5, 2, 3, 5, 10, 20, 30 h). The main disc was rotated at 350 rpm while the vials were rotated at 800 rpm in reverse.

Synthesis of SiBCN-Ta₄HfC₅ powder and bulk ceramics

In this stage, c-Si, h-BN, graphite with a molar ratio of = 2: 1: 3, and 2.5 wt%, 5 wt%, 10 wt% Ta₄HfC₅ nanocrystals were put into ball milling tanks. Before the milling process, the rotation speed of the main disc was set at 350 rpm while the vials were rotated at 600 rpm in reverse. In this scene, the effective milling time of 20 h could ensure a well-defined microstructure of the mixtures^[32-33]. The steps of mixing, storage and transportation are performed in high purity Ar.

SiBCN-Ta₄HfC₅ mixed powders were loaded into a graphite mould with a diameter of 36 mm, and then sintered via the hot-pressing sintering system (50-250T model, AVS company, USA). The sintering was conducted at a temperature of 1900 °C and holding time for 1 h under an axial pressure of 60 MPa. The

content of Ta₄HfC₅ in SiBCN-Ta₄HfC₅ composite ceramics is 0 wt%, 2.5 wt%, 5 wt%, 10 wt% and 15 wt%, respectively.

Characterization

The phase composition of the samples was measured by X'PERT X-ray diffractometer purchased from Panalytical Company of Netherlands. The scanning speed is 10°/min and the scanning range is 10°-90°. The morphologies of the samples were observed by using NanoLab 600i scanning electron microscope produced by FEI company. Tecnal G² F20 transmission electron microscope from FEI company was used to observe the microstructure of Ta₄HfC₅ and SiBCN-Ta₄HfC₅ powders. The microstructure and element distribution of the SiBCN-Ta₄HfC₅ composite ceramics were investigated by using Talos f200x transmission electron microscope produced by FEI company. The Raman spectra were collected via an inVia-Reflex testing system manufactured by RENISHAW company, with the excitation wavelength of 785 nm.

Results And Discussion

Synthesis and characterization of nano Ta₄HfC₅ powder

Prior to mechanical alloying, the powder mixture of the TaC-HfC shows sharp diffraction peaks (Fig. 1). After 0.5 h of milling, the intensities of the corresponding diffraction peaks are reduced and the full width at half maximum (FWHM) becomes wider. This should be argued to the grain refinement of TaC and HfC. As the milling time further raises to 1 ~ 5 h, these crystalline peaks decrease gradually and finally disappear after 10 h of milling. At this stage, the decrease of nanocrystalline peak intensities and the increase of FWHM are mainly due to the gradual solid solution of TaC and HfC. Interestingly, the single-phase Ta₄HfC₅ solid solution is obtained after mechanical alloying for 10 h. Further prolonging the milling time to 20 ~ 30 h, the diffraction peaks of the as-prepared Ta₄HfC₅ gradually decrease, implying the grain refinement of Ta₄HfC₅ (Fig. 2).

After mechanical alloying, the diffraction peaks of the as-prepared Ta₄HfC₅ shifting to the small angle direction must result from the radius difference between Hf and Ta, which can be depicted by the Vegard's law:

$$a = a_1 c_1 + a_2 c_2 \quad (1)$$

Where a , a_1 and a_2 represent the lattice constant of the new forming solid solution, and the two starting components, respectively. The c_1 and c_2 represent the concentration of the two starting components, respectively [34-36]. The radius of the Hf is bigger than that of Ta. Thus, the short-range diffusion of Hf atoms into the interstitial sites of Ta can lead to the expansion of TaC lattice.

TEM analyses confirm the raw materials of TaC and HfC powders both have relatively large grain size [Fig. 3(a) and (b)]. Besides, the corresponding SAED pattern displays some diffraction spots and rings of HfC and TaC [Fig. 3(c)]. After ball milling for only 0.5 h, the grain size of TaC and HfC decreases obviously and some diffraction spots of TaC and HfC have disappeared [Fig. 3(d-f)]. Notably, at this milling time, mechanical alloying has induced many structural defects in both TaC and HfC, which can provide convenient channel for Hf atoms diffusing inward. With the progressing milling of 30 h, only pure Ta₄HfC₅ nanocrystals are obtained without any trace of HfC or below the limits of detection [Fig. 3(g-i)]. For pure TaC ball-milled for 30 h [Fig. 3(j-l)], SAED pattern with bright-spots and narrow-rings verifies the well-defined crystalline phase of TaC.

The SEM surface morphologies in Fig. 4(a) further ensure that the raw materials of TaC-HfC powder mixture have larger particle size. Nevertheless, after mechanical alloying for 0.5 h, the particle size of the powder mixture decreases obviously, which is mainly composed of nano-particles [Fig. 4(b)]. With the progress of mechanical alloying (1.5–30 h), these particles are continuously deformed, crushed and cold sintered; however, the morphologies of the resulting particles are almost unchanged. The EDS maps in Fig. 4(f)-(i) confirm that the Ta, Hf and C atoms distribute uniformly after 30 h of milling, suggesting a good solid solubility of Hf into TaC.

Figure 5 shows the XRD patterns of the in situ SiBCN-Ta₄HfC₅ amorphous-nanocrystalline composite powder with different Ta₄HfC₅ content. After 20 h of mechanical alloying, the lattice structure of c-Si, h-BN and graphite was destroyed to form amorphous SiBCN. Besides, the broad diffraction peaks of Ta₄HfC₅ were observed, and these peak intensities gradually increase with the increase of Ta₄HfC₅ content. Confidently, the nano Ta₄HfC₅ does not react with other components of SiBCN and still presents the form of nanocrystals ~ 3–5 nm in the amorphous matrix after mechanical alloying (Fig. 6).

The formation mechanisms of the mechanical alloying derived nano Ta₄HfC₅ are elaborated in Fig. 7. During the mechanical alloying process, the sample particles are continuously deformed, crushed and cold sintered under mechanical impact conditions, which led to grain refinement and microstrain occurring in the crystal grains. The dislocation density can be represented by the following equation [37]:

$$\rho_D = 2\sqrt{3} \frac{(\varepsilon^2)^{\frac{1}{2}}}{Db} \quad (2)$$

Where ε is the microstrain, D is the grain size, and b is the Burgers vector. According to formula (2), larger microstrain and smaller grain size lead to higher dislocation density in the crystal. Besides, the decrease in grain size results in an increase in surface area per unit volume. Higher surface energy provides a driving force for diffusion, while more defects provide channels for atom diffusion. Therefore, a uniform solid solution of Ta₄HfC₅ was formed.

Microstructural evolution and mechanical properties of as-sintered SiBCN-Ta₄HfC₅ composite ceramics

After reactive hot-pressing sintering, SiBCN-Ta₄HfC₅ composite ceramics mainly consist of BN(C), β -SiC, α -SiC and Ta₄HfC₅ (Fig. 8). Obviously, the intensity of the diffraction peaks of the Ta₄HfC₅ is positively correlated with the content of Ta₄HfC₅. Interestingly, with the increase of Ta₄HfC₅ content, the diffraction peaks of α -SiC decrease while the diffraction peaks of β -SiC increase. These means that the in situ Ta₄HfC₅ affects the $\beta \rightarrow \alpha$ transition of SiC.

Figure 9 exhibits the Raman spectra of the as-sintered SiBCN-Ta₄HfC₅ composite ceramics with various Ta₄HfC₅ content. Two Raman peaks in a range of 1250–1750 cm⁻¹ are gradually enhanced with the increase content of the in situ Ta₄HfC₅. The emergence of Raman peak at 1374 cm⁻¹ results from the D-side peak edge of graphite and the scattering peak of h-BN^[5]. However, the generation of Raman peak at 1588 cm⁻¹ should be assigned to the G-side peak of graphite^[38].

After hot-pressing sintering, amorphous SiBCN has crystallized to product turbostratic BN(C) and nano SiC (Fig. 10). For pure SiBCN, BN(C) phase is distributed at the grain boundaries of SiC grains. Besides, the Si elements are mainly distributed in SiC grains, while B, C and N elements are distributed in the form of BN(C) phase at SiC grain boundaries. With 2.5 wt% Ta₄HfC₅ addition, most of the Ta₄HfC₅ ~ 10 nm are distributed in BN(C) phase in the form of nanocrystals (Fig. 11). The Ta₄HfC₅ grains are thereby separated by BN(C). This structure is beneficial to the grain refinement of Ta₄HfC₅ and constrains short-range diffusion of the atoms. The EDS maps of the selective region in Ta₄HfC₅-BN(C) clearly show that the Ta, Hf and some C elements are distributed in Ta₄HfC₅ phase, while the rest of C elements are distributed in BN(C) phase (Fig. 12). With 10 wt% Ta₄HfC₅ addition, a part of nano Ta₄HfC₅ ~ 10 nm is still uniformly distributed in BN(C), while other nano Ta₄HfC₅ > 10 nm is randomly distributed in the ceramic matrix (Fig. 13). The microstructural evolution diagram of the SiBCN-Ta₄HfC₅ composite ceramics with different Ta₄HfC₅ content is displayed in Fig. 14.

The flexural strength and fracture toughness of the as-sintered SiBCN-Ta₄HfC₅ composite ceramics are shown in Fig. 15. Apparently, the introduction of Ta₄HfC₅ nanocrystals has effectively improved the flexural strength and fracture toughness of the SiBCN ceramics. For pure SiBCN ceramics, they only show flexural strength of 156.1 MPa and fracture toughness of 1.82 MPa·m^{1/2}, respectively. With 10 wt% Ta₄HfC₅ addition, the composite ceramics possess optimized flexural strength reaching to 344.1 MPa, while the composite ceramics with 5 wt% Ta₄HfC₅ obtain fracture toughness of 4.52 MPa·m^{1/2}.

Conclusion

In this study, SiBCN-Ta₄HfC₅ composite ceramics were prepared by two-step mechanical alloying combined with reactive hot-pressing sintering. After the above analysis, the following conclusions can be

drawn:

(1) In the initial step of mechanical alloying of 30 h, TaC-HfC powder mixture are crushed, cold sintered and interdiffused, and finally form Ta₄HfC₅ nanocrystalline. After the second step of milling for 20 h, a hybrid structure of amorphous SiBCN and nano Ta₄HfC₅ can be obtained. The lattice structures of C-Si, h-BN and graphite were destroyed to form amorphous structures. However, Ta₄HfC₅ is uniformly distributed in amorphous powder in the form of nanocrystals.

(2) After reactive hot-pressing sintering, SiBCN-Ta₄HfC₅ composite ceramics mainly contain Ta₄HfC₅, BN(C), β-SiC and α-SiC. The Ta₄HfC₅ still exists in the form of nanocrystalline and does not react with the SiBCN matrix composition. With only 2.5 wt% Ta₄HfC₅ addition, nano Ta₄HfC₅ is preferentially distributed in BN(C) phase; however, it tends to both distribute in BN(C) phase and ceramic matrix when 10 wt% Ta₄HfC₅ is adopted.

(3) The introduction of the Ta₄HfC₅ nanocrystals can effectively improve the flexural strength and fracture toughness of SiBCN ceramics due to the grain refinement and uniform distribution of nano Ta₄HfC₅. SiBCN ceramics with 10 wt% Ta₄HfC₅ present optimized flexural strength of 344.1 MPa, while composite ceramics with 5 wt% Ta₄HfC₅ obtain fracture toughness of 4.52 MPa·m^{1/2}.

Declarations

Acknowledgements

Financial support from the National Natural Science Foundation of China under grant numbers of 51621091, 51472059, 51225203 and 51272300 is much appreciated. This work is also funded by National Key Research and Development Program (Grant No. 2017YFB0310400), Postdoctoral Innovative Talents Support Program with Grant No BX20190095 and China Postdoctoral Science Foundation under grant numbers of 2019M660072.

References

- [1] Z. Zhang, X. Duan, B. Qiu, Z. Yang, D. Cai, P. He, D. Jia, Y. Zhou, Preparation and anisotropic properties of textured structural ceramics: A review, *Journal of Advanced Ceramics* 8 (2019) 289-332.
- [2] R. Riedle, A. Kienzle, W. Dressler, L. Ruwisch, J. Bill, F. Aldinger, A silicoboron carbonitride ceramic stable to 2000 °C, *Nature* 382 (1996) 796-798.
- [3] R. Riedle, L.M. Ruswisch, L. An, R. Raj, Amorphous silicoboron carbonitride ceramic with very high viscosity at temperatures above 1500°C, *Journal of the American Ceramic Society* 81 (2005) 3341-3344.
- [4] N.V.R. Kumar, S. Prinz, C. Ye, A. Zimmermann, F. Aldinger, F. Berger, K. Müller, Crystallization and creep behavior of Si-B-C-N ceramics, *Acta Materialia* 53 (2005) 4567-4578.

- [5] N. Liao, D. Jia, Z. Yang, Y. Zhou, Y. Li, Enhanced thermal shock and oxidation resistance of $\text{Si}_2\text{BC}_3\text{N}$ ceramics through MWCNTs incorporation. [Journal of Advanced Ceramics](#) 7 (2018) 276-288.
- [6] N. Liao, D. Jia, Z. Yang, Y. Zhou, Enhanced mechanical properties and thermal shock resistance of $\text{Si}_2\text{BC}_3\text{N}$ ceramics with SiC coated MWCNTs. [Journal of Advanced Ceramics](#) 8 (2019) 121-132.
- [7] J. Wang, Z. Yang, X. Duan, D. Jia, Y. Zhou, Microstructure and mechanical properties of $\text{SiC}_f/\text{SiBCN}$ ceramic matrix composites. [Journal of Advanced Ceramics](#) 4 (2015) 31-38.
- [8] T.G. Babu, R. Devasia, Simple and low-cost synthetic route for SiBCN ceramic powder from a boron modified cyclotrisilazane, [Journal of the American Ceramic Society](#) 102 (2019) 476-489.
- [9] C. Song, X. Liu, F. Ye, Y. Liu, L. Cheng, Mechanical and dielectric properties of $\text{SiC}_f/\text{BN}/\text{SiBCN}$ composites via different synthesis technologies, [Journal of the European Ceramic Society](#) 39 (2019) 4417-4423.
- [10] D. Jia, B. Liang, Z. Yang, Z. Yu, Metastable Si-B-C-N ceramics and their matrix composites developed by inorganic route based on mechanical alloying: Fabrication, microstructures, properties and their relevant basic scientific issues, [Progress in Materials Science](#) 98 (2018) 1-67.
- [11] D. Li, Q. Li, J. Yuan, Z. Yang, D. Jia, D. Cai, S. Wang, Y. Zhou, D. Yu, Y. Tian, Effects of high pressure on the low-temperature sintering of dense amorphous SiBCN monoliths, [Journal of the European Ceramic Society](#) 38 (2018) 3777-3786.
- [12] P. Zhang, D. Jia, Z. Yang, X. Duan, Y. Zhou, Progress of a novel non-oxide Si-B-C-N ceramic and its matrix composites, [Journal of Advanced Ceramics](#) 1 (2012) 157-178.
- [13] J. Wang, X. Duan, Z. Yang, D. Jia, Y. Zhou, Ablation mechanism and properties of $\text{SiC}_f/\text{SiBCN}$ ceramic composites under an oxyacetylene torch environment, [Corrosion Science](#) 82 (2014) 101-107.
- [14] D. Li, Z. Yang, D. Jia, X. Duan, P. He, Y. Zhou, Ablation behavior of graphene reinforced SiBCN ceramics in an oxyacetylene combustion flame, [Corrosion Science](#) 100 (2015) 85-100.
- [15] N. Liao, D. Jia, Z.H. Yang, B. Niu, Y. Zhou, Y. Li, Enhanced mechanical properties, thermal shock resistance and ablation resistance of $\text{Si}_2\text{BC}_3\text{N}$ ceramics with nano ZrB_2 addition, [Journal of the European Ceramic Society](#) 39 (2019) 846-859.
- [16] B. Feng, Y. Zhang, B. Li, Medium-temperature sintering efficiency of ZrB_2 ceramics using polymer-derived SiBCN as a sintering aid, [Journal of the European Ceramic Society](#) 102 (2019) 855-866.
- [17] B. Wang, Z. Yang, D. Li, D. Cai, B. Niu, J. Guan, D. Jia, Y. Zhou, Effects of TaC addition on microstructure and mechanical properties of SiBCN composite ceramics, [Ceramics International](#). 45 (2019) 22138-22147..

- [18] M. Sun, R. Fu, J. Chen, Fabrication and microstructures of functional gradient SiBCN-Nb composite by hot pressing, *Materials Characterization* 114 (2019) 115-121.
- [19] B. Feng, Y. Zhang, B. Li, S. Hu, Medium-temperature sintering efficiency of ZrB₂ ceramics using polymer-derived SiBCN as a sintering aid, *Journal of the American Ceramic Society*. 102 (2019) 855–866.
- [20] S. Wang, Y. Zhang, S. Yong, X. Yao, Y. Ming, Synthesis and characteristic of SiBCN/HfN ceramics with high temperature oxidation resistance, *Journal of Alloys and Compounds*. 685 (2016) 828–835.
- [21] B. Liang, Z. Yang, D. Jia, S. Guo, Q. Zhu, X. Liao, Y. Miao, Q. Zhang, Y. Zhou, Densification, microstructural evolution and mechanical properties of Si-B-C-N monoliths with LaB₆ addition, *Journal of Alloys and Compounds* 696 (2017) 1090-1095.
- [22] B. Liang, Z. Yang, Y. Miao, Q. Zhu, X. Liao, Q. Li, Z. Tian, D. Jia, Y. Zhou, Si-B-C-N monoliths with LaB₆-induced well-developed BN(C) flakes, *Materials Letters* 187 (2017) 36-39.
- [23] B. Liang, Z. Yang, Y. Miao, Q. Li, Q. Zhu, X. Liao, D. Jia, Y. Zhou, Microstructural evolution, mechanical and thermal properties of LaB₆ embedded in Si-B-C-N prepared by spark plasma sintering, *Ceramics International*. 43 (2017) 4814-4820.
- [24] Y. Miao, Z. Yang, B. Liang, Q. Li, Q. Chen, D. Jia, Y.B. Cheng, Y. Zhou, A novel in situ synthesis of SiBCN-Zr composites prepared by a sol-gel process and spark plasma sintering, *Dalton Transactions*. 45 (2016) 12739-12744.
- [25] Y. Miao, Z. Yang, J. Rao, X. Duan, P. He, D. Jia, Y. Cheng, Y. Zhou, Influence of sol-gel derived ZrB₂ additions on microstructure and mechanical properties of SiBCN composites, *Ceramics International*. 43 (2017) 4372-4378.
- [26] Y. Miao, Z. Yang, Q. Zhu, B. Liang, L. Quan, T. Zhuo, D. Jia, Y.B. Cheng, Z. Yu, Thermal ablation behavior of SiBCN-Zr composites prepared by reactive spark plasma sintering, *Ceramics International*. 43 (2017) 7978-7983.
- [27] Agte C, Alterthum H, Investigations of the High-Melting Carbide Systems Connected with Problem of the Carbon Melting, *Z. Techn. Phys.* 11 (1930) 182.
- [28] Andrievskii R A, Strel'Nikova N S, Poltoratskii N I, Melting point in systems ZrC-HfC, TaC-ZrC, TaC-HfC, *Soviet Powder Metallurgy & Metal Ceramics*. 6 (1967) 65-67.
- [29] E. P. Simonenko, N. A. Ignatov, N. P. Simonenko, Yu. S. Ezhov, V. G. Sevastyanov, N. T. Kuznetsov, Zirconium Carbide Ta₄ZrC₅ and Tantalum–Hafnium Carbide Ta₄HfC₅ via Sol–Gel Technology, *Synthesis and Properties of Inorganic Compounds*. 56 (2011) 1763-1769.

- [30] Y. Lu, Y. Sun, T. Zhang, F. Chen, L. Ye, T. Zhao, Polymer-derived Ta₄HfC₅ nanoscale ultrahigh-temperature ceramics: Synthesis, microstructure and properties, *Journal of the European Ceramic Society*. 39 (2019) 205-211.
- [31] Osama Gaballa, B.A. Cook, A.M. Russell, Reduced-temperature processing and consolidation of ultra-refractory Ta₄HfC₅, *Int. Journal of Refractory Metals and Hard Materials*. 41 (2013) 293-299
- [32] N. Liao, D. Jia, Z. Yang, Y. Zhou, Y. Li, X. Jia, Strengthening and toughening effects of MWCNTs on Si₂BC₃N ceramics sintered by SPS technique, *Materials Science and Engineering A*. 710 (2018) 142-150.
- [33] N. Liao, D. Jia, Z. Yang, Z. Yu, Y. Li, Mechanical properties and thermal shock resistance of Si₂BC₃N ceramics with ternary Al₄SiC₄ additive, *Ceramics International*. 44 (2018) 9009-9017.
- [34] H. Chen, B. Tang, C. Zhong, Y. Yuan, Y. Tan, S. Zhang, The dielectric constant and quality factor calculation of the microwave dielectric ceramic solid solutions, *Ceramics International*. 43(2017) 7383-7386.
- [35] Q. Hang, Z. Xing, X. Zhu, M. Yu, Y. Song, J. Zhu, Z. Liu, Dielectric properties and related ferroelectric domain configurations in multiferroic BiFeO₃-BaTiO₃ solid solutions, *Ceramics International*. 38 (2012) S411-S414.
- [36] E. Antolini, Li₂O evaporation from Li_xCo_{1-x}O solid solutions at 1200 degrees C, *Ceramics International*. 27 (2001) 675-679.
- [37] K. Zaara, M. Cheinggui, V. Optasanu, M. Khitouni, Solid solution evolution during mechanical alloying in Cu-Nb-Al compounds, *International Journal of Minerals Metallurgy and Materials*. 26 (2019) 1129-1139.
- [38] D. Li, Z. Yang, D. Jia, S. Wang, X. Duan, B. Liang, Q. Zhu, Y. Zhou, Structure evolution, amorphization and nucleation studies of carbon-lean to -rich SiBCN powder blends prepared by mechanical alloying, *RSC Advance* 6 (2016) 48255-48271.

Figures

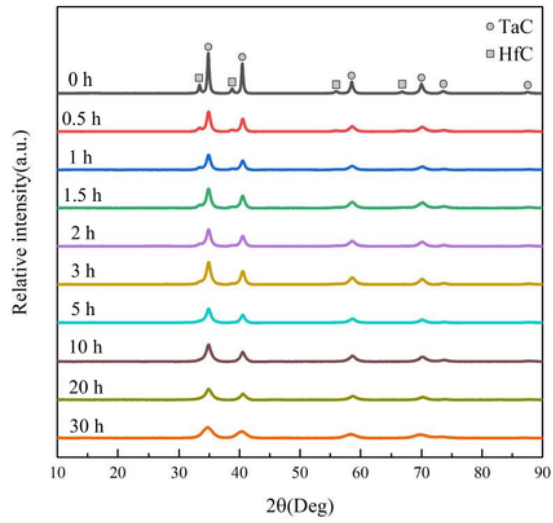


Fig. 1 The XRD patterns of the TaC-HfC powder mixture after mechanical alloying for different time.

Figure 1

The XRD patterns of the TaC-HfC powder mixture after mechanical alloying for different time.

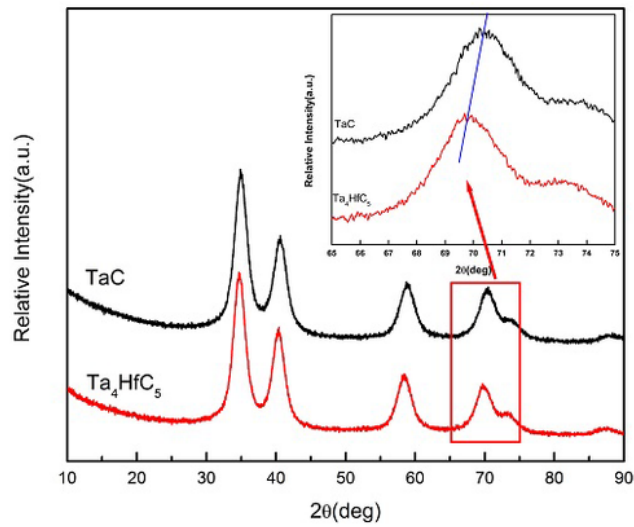


Fig. 2 The XRD patterns of pure TaC powder and TaC-HfC powder mixture after mechanical alloying for 30 h, inserted is the magnifying picture.

Figure 2

The XRD patterns of pure TaC powder and TaC-HfC powder mixture after mechanical alloying for 30 h, inserted is the magnifying picture.

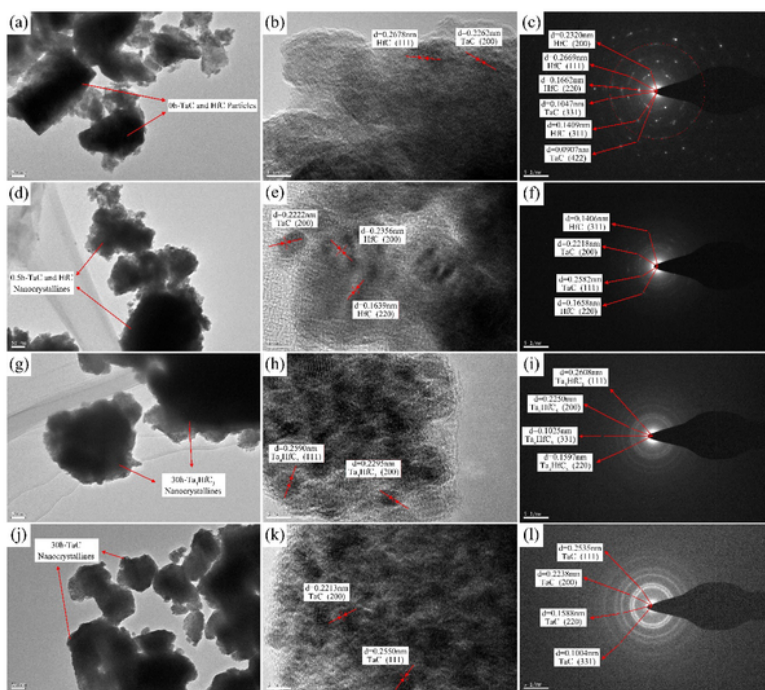


Fig. 3 The TEM, HRTEM and electron diffraction pattern (SAED) images of the pure TaC powder and HfC-TaC powder mixture after mechanical alloying for different time. (a-e) HfC-TaC, 0 h; (d-f) HfC-TaC, 0.5 h; (g-i) HfC-TaC, 30 h; (j-l) pure TaC powder, 30 h.

Figure 3

The TEM, HRTEM and electron diffraction pattern (SAED) images of the pure TaC powder and HfC-TaC powder mixture after mechanical alloying for different time. (a-c) HfC-TaC, 0 h; (d-f) HfC-TaC, 0.5 h; (g-i) HfC-TaC, 30 h; (j-l) pure TaC powder, 30 h.

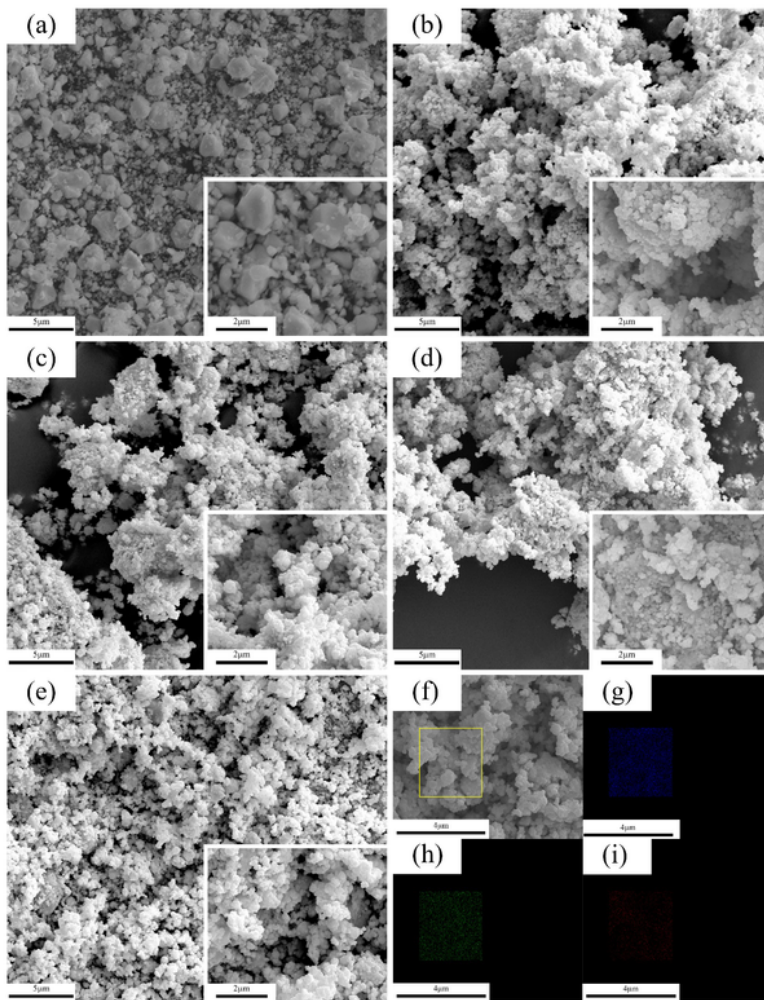


Fig.4 The SEM surface images of TaC-HfC mixed powders after mechanical alloying for different time. (a) 0 h; (b) 0.5 h; (c) 1.5 h; (d) 20 h; (e, f) 30 h; (g-i) the corresponding element maps, the inserted are the magnifying SEM images.

Figure 4

The SEM surface images of TaC-HfC mixed powders after mechanical alloying for different time. (a) 0 h; (b) 0.5 h; (c) 1.5 h; (d) 20 h; (e, f) 30 h; (g-i) the corresponding element maps, the inserted are the magnifying SEM images.

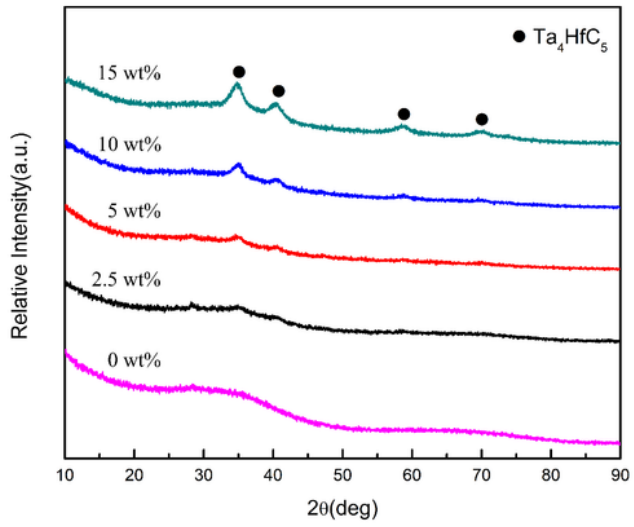


Fig. 5 The XRD patterns of in situ SiBCN-Ta₄HfC₅ amorphous-nanocrystalline composite powder with different Ta₄HfC₅ content.

Figure 5

The XRD patterns of in situ SiBCN-Ta₄HfC₅ amorphous-nanocrystalline composite powder with different Ta₄HfC₅ content.

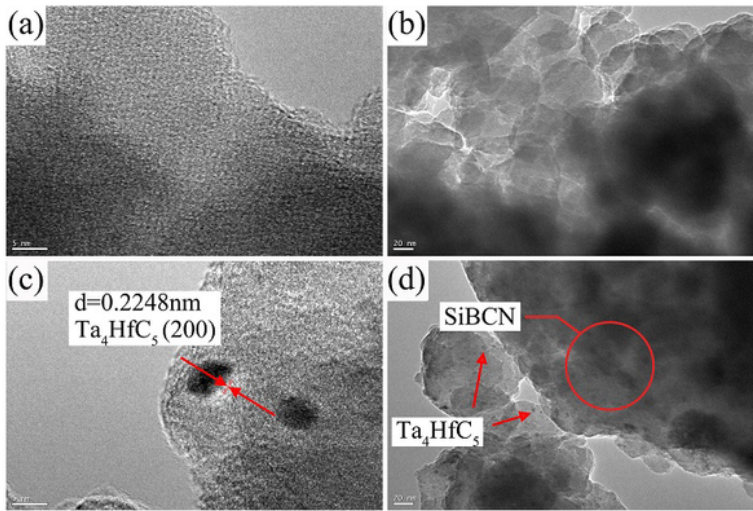


Fig. 6 The TEM and HRTEM images of the (a-b) SiBCN amorphous powder and (c-d) SiBCN-Ta₄HfC₅ amorphous-nanocrystalline composite powder.

Figure 6

The TEM and HRTEM images of the (a-b) SiBCN amorphous powder and (c-d) SiBCN-Ta₄HfC₅ amorphous-nanocrystalline composite powder.

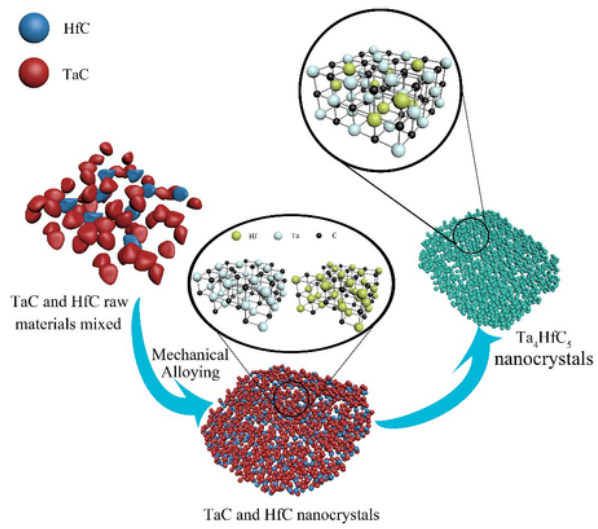


Fig. 7 The formation mechanisms of the nano Ta_4HfC_5 during mechanical alloying.

Figure 7

The formation mechanisms of the nano Ta_4HfC_5 during mechanical alloying.

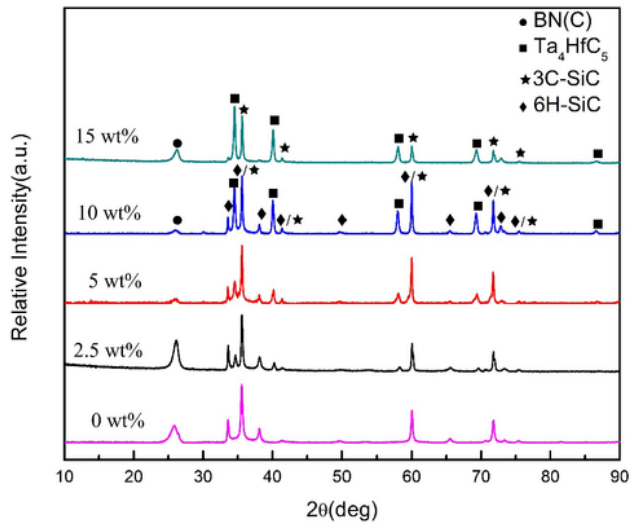


Fig. 8 The XRD patterns of the as-sintered SiBCN-Ta₄HfC₅ composite ceramics with different Ta₄HfC₅ content.

Figure 8

The XRD patterns of the as-sintered SiBCN-Ta₄HfC₅ composite ceramics with different Ta₄HfC₅ content.

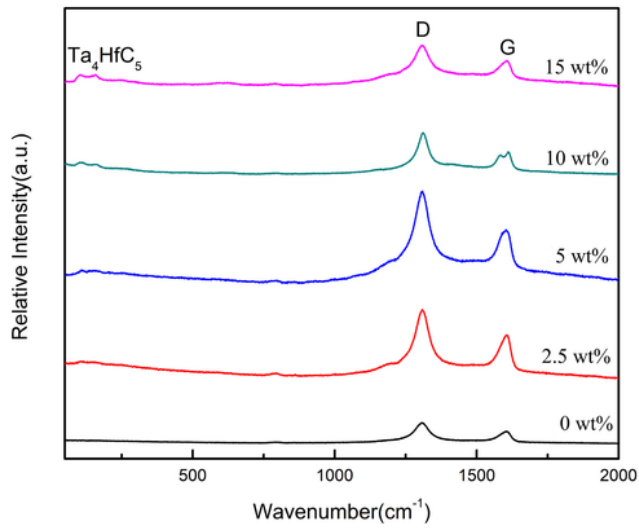


Fig. 9 The Raman spectra of the as-sintered SiBCN-Ta₄HfC₅ composite ceramics with different Ta₄HfC₅ content.

Figure 9

The Raman spectra of the as-sintered SiBCN-Ta₄HfC₅ composite ceramics with different Ta₄HfC₅ content.

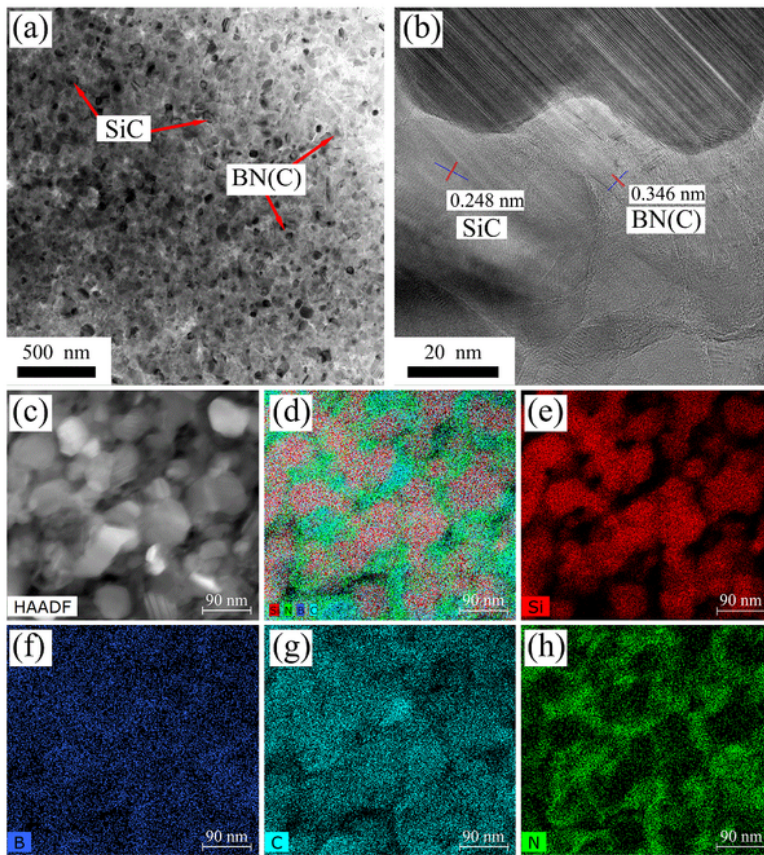


Fig. 10 The TEM and HEM images of the pure SiBCN ceramics. (a-b) Bright-field images; (c)-(j) HAADF-STEM image and corresponding EDS maps.

Figure 10

The TEM and HEM images of the pure SiBCN ceramics. (a-b) Bright-field images; (c)-(j) HAADF-STEM image and corresponding EDS maps.

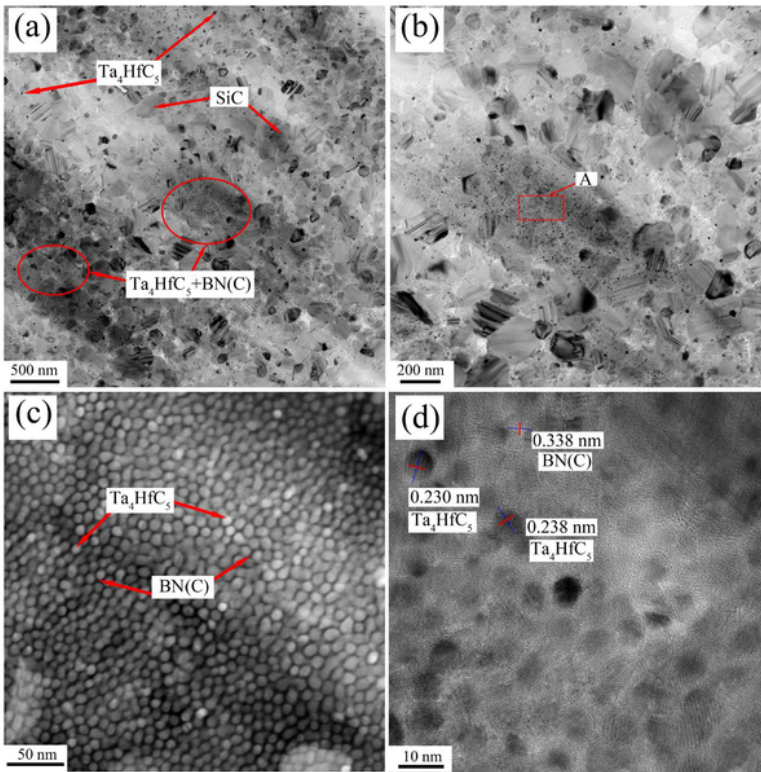


Fig. 11 The TEM and HRTEM images of the SiBCN-Ta₄HfC₅ composite ceramics with 2.5 wt% Ta₄HfC₅. (a-b) Bright-field images; (c) Magnifying TEM image of area A; (d) HRTEM image of area A.

Figure 11

The TEM and HRTEM images of the SiBCN-Ta₄HfC₅ composite ceramics with 2.5 wt% Ta₄HfC₅. (a-b) Bright-field images; (c) Magnifying TEM image of area A; (d) HRTEM image of area A.

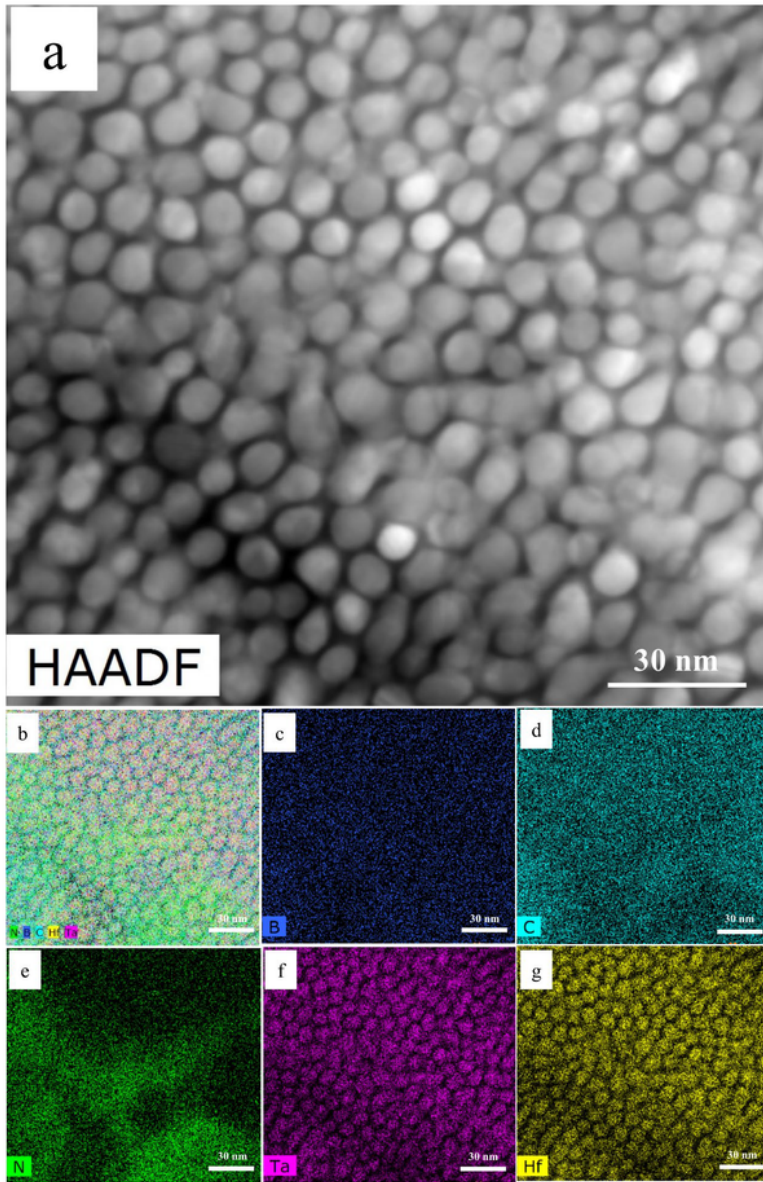


Fig.12 The selective EDS maps of Ta_4HfC_5 distributed within BN(C) region for composite ceramics with 2.5 wt% Ta_4HfC_5 .

Figure 12

The selective EDS maps of Ta_4HfC_5 distributed within BN(C) region for composite ceramics with 2.5 wt% Ta_4HfC_5 .

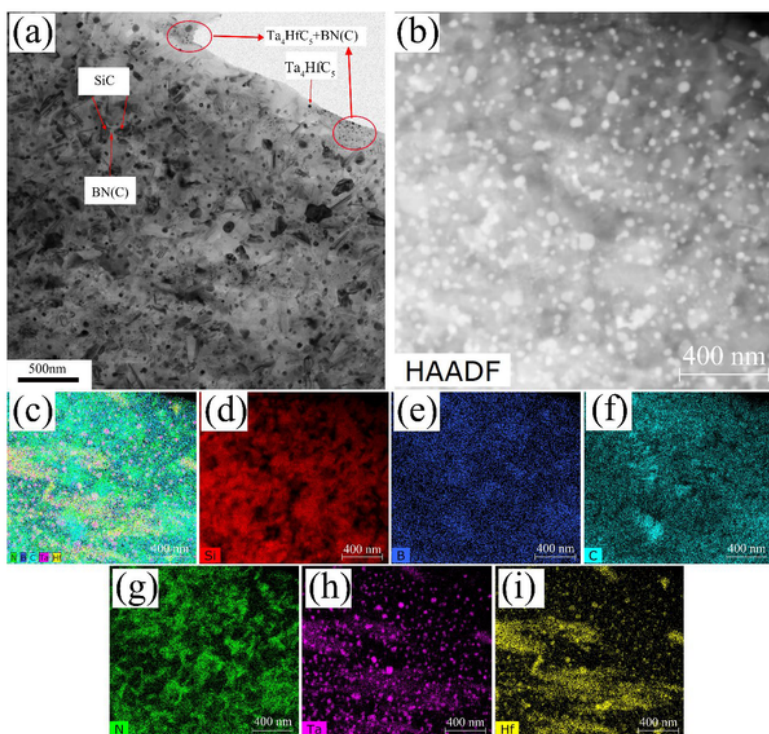


Fig. 13 The TEM images and EDS maps of the SiBCN-Ta₄HfC₅ composite ceramics with 10 wt% Ta₄HfC₅. (a) Bright-field TEM image; (b) STEM image; (d)-(j) EDS maps.

Figure 13

The TEM images and EDS maps of the SiBCN-Ta₄HfC₅ composite ceramics with 10 wt% Ta₄HfC₅. (a) Bright-field TEM image; (b) STEM image; (d)-(j) EDS maps.

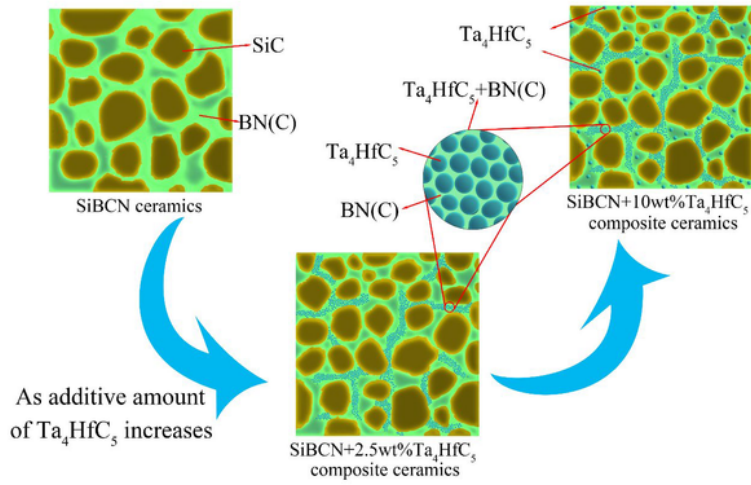


Fig.14 The schematic illustrating the microstructure evolution of Ta₄HfC₅ distribution in composite ceramics with different Ta₄HfC₅ addition.

Figure 14

The schematic illustrating the microstructure evolution of Ta₄HfC₅ distribution in composite ceramics with different Ta₄HfC₅ addition.

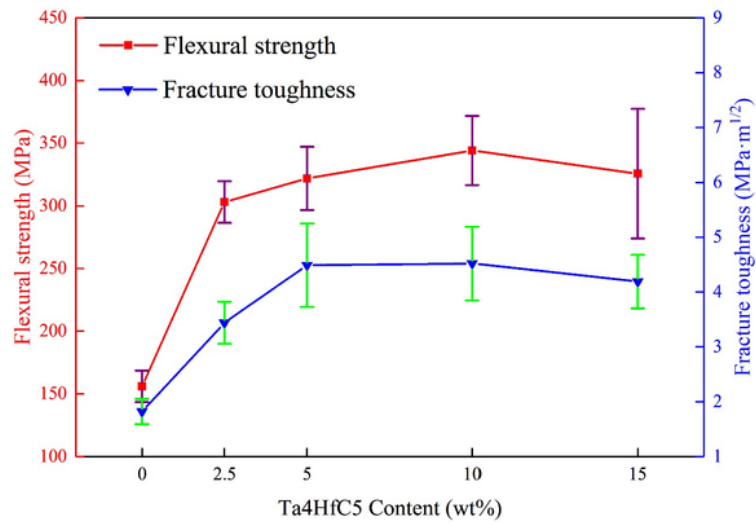


Fig. 15 The flexural strength and fracture toughness of the as-sintered SiBCN-Ta₄HfC₅ composite ceramics with different content of Ta₄HfC₅.

Figure 15

The flexural strength and fracture toughness of the as-sintered SiBCN-Ta₄HfC₅ composite ceramics with different content of Ta₄HfC₅.